ACS Energy Letters

http://pubs.acs.org/journal/aelccp

LETTER

Enhanced SOC Estimation for LFP Batteries: A Synergistic Approach Using Coulomb Counting Reset, Machine Learning, and Relaxation

Yunhong Che,[§] Le Xu,[§] Remus Teodorescu, Xiaosong Hu,* and Simona Onori*

Cite This: *ACS Energy Lett.* 2025, 10, 741−749

Read Online

ACCESS | Metrics & More | Article Recommendations | Supporting Information

ABSTRACT: State-of-charge (SOC) estimation for lithium−iron phosphate (LFP) batteries is a challenging task due to their path-dependent behavior, flat open circuit voltage (OCV) characteristics, and hysteresis effects. This work proposes a machine-learning-based SOC estimation method designed for onboard applications, addressing the challenges of SOC initialization when using the Coulomb counting method. The proposed approach relies on low sampling frequency measurements during short-term rest periods. Experiments were conducted on LFP 26650 cells across more than 430 working conditions, involving four temperatures, three current rates, four cycling scenarios, with various resting periods at different SOC levels. A comprehensive analysis of SOC estimation errors, including initial value errors, sensor noise, and sampling frequency, is provided. Using relaxation voltage data recorded at intervals as short as 1 min, the SOC resetting estimation solution proposed in this paper achieves mean absolute errors lower than 3.25%, demonstrating its potential for real-world applications. This solution can be readily integrated into existing battery management systems.

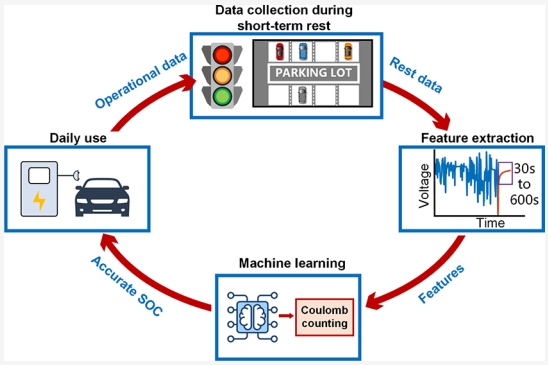

Lithium-ion batteries are the most widely used electrochemical energy storage devices in consumer electronics, electrified transportation, and grid applications due to their high energy density, continuously decreasing cost, and long cycle life.[1,2] Lithium−iron phosphate (LFP) batteries, which utilize graphite anodes and LFP cathodes, are free of cobalt and nickel. Due to its excellent thermal stability and low risk of thermal runaway, LFP is considered one of the safest cathode materials, providing enhanced safety.[3] This combination of safety, long cycle life, and stable performance makes LFP batteries a strong candidate for use in electric vehicles, energy storage systems, and other applications where safety and durability are critical.[4,5] In addition, the abundance of phosphate resources ensures a stable and sustainable supply chain for LFP batteries, contributing to their growing adoption. These advantages have led to LFP batteries capturing over 30% of the market share in cathode chemistries,[6] a figure that continues to rise.

A battery management system (BMS) is designed to ensure functional, safe, and reliable operation of the system when used in real time.[7] One of the critical tasks performed by the BMS is state-of-charge (SOC) estimation, which becomes particularly challenging for LFP batteries.

This difficulty arises from several factors, including hysteresis effects, path-dependent dynamics, and the flat characteristics of the open-circuit voltage (OCV). Accurate SOC estimation is vital for optimizing battery performance, extending battery life, and preventing potential safety issues, making it a key focus area in the development of advanced BMS technologies.[8]

Hysteresis in LFP batteries refers to the voltage gap observed between the charging and discharging processes at similar SOC levels.[9] Several factors contribute to hysteresis in LFP batteries, including thermodynamic effects, mechanical stress, and microscopic distortions within the active material particles induced by dopants.[10] Hysteresis in LFP batteries has

Received: November 19, 2024
Accepted: December 16, 2024

Downloaded via STANFORD UNIV on January 13, 2025 at 20:36:16 (UTC).
See https://pubs.acs.org/sharingguidelines for options on how to legitimately share published articles.

© XXXX American Chemical Society

https://doi.org/10.1021/acsenergylett.4c03223
ACS Energy Lett. 2025, 10, 741−749

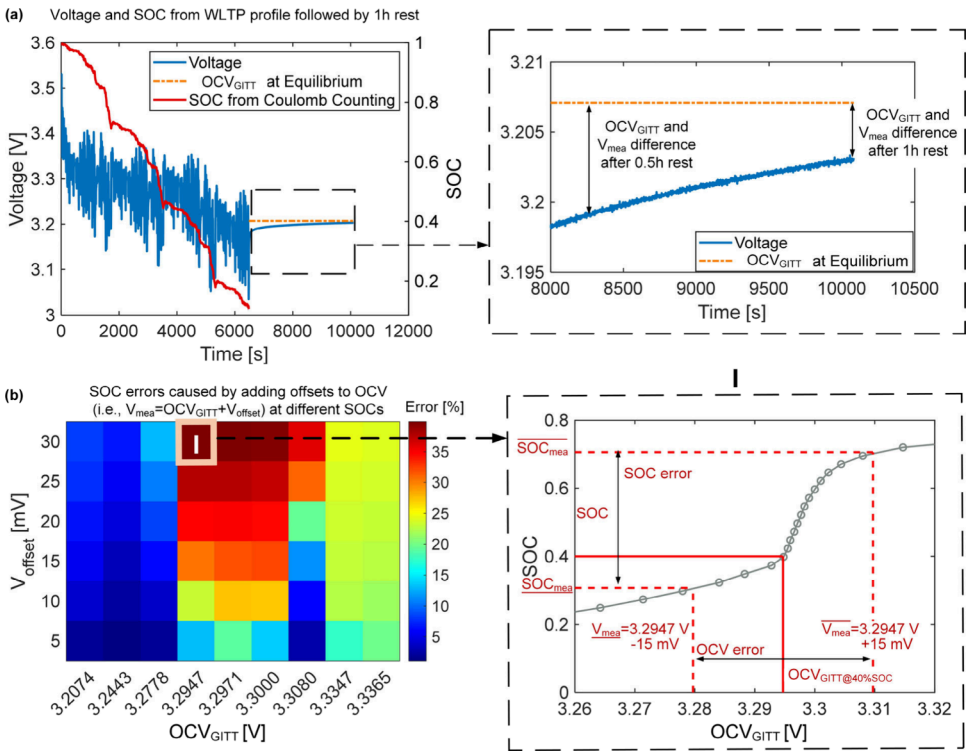

Figure 1. Analysis of error sources for inaccurate initial SOC values. (a) Voltage and SOC from the WLTP profile followed by a 1 h rest. The orange dash line represents the OCV_{GITT} when the LFP battery is at equilibrium state. The solid red line represents the SOC calculated from the Coulomb counting method. In the zoomed-in plot, the blue line represents the voltage trajectory during the 1 h rest period after the end of discharge. The difference between the measured voltage V_{mea} and the OCV_{GITT} decreases as the resting time increases, indicating that a long-time rest period is needed to accurately determine the battery SOC using the OCV−SOC inversion. (b) SOC errors caused when voltage offset noise is applied to the OCV_{GITT} at different SOC levels. Insert I shows SOC errors when 30 mV voltage offset is added to the OCV_{GITT} values of 3.2947 V (corresponding to 40% SOC).

been modeled in two main ways in the literature. The first method employs an empirical approach, using a first-order ordinary differential equation to characterize the dynamics. This model captures the dynamic response of the battery by relating the voltage gap between charging and discharging processes to changes in SOC and current, allowing for a more accurate representation of hysteresis behavior.[11] The parameters of this model must be carefully calibrated using data from both major and minor loop experiments. In current studies, both equivalent circuit models (ECMs)[12] and physics-based models[13] have integrated this empirical equation to improve the accuracy of LFP battery modeling.

The second type of method proposed in the literature utilizes a hybrid approach that integrates an electrochemical model describing the two-phase transition operation in the positive electrode,[14] with a machine learning component. This component, designed to capture the hysteresis effects and path-dependent dynamics of the battery, is trained on data that includes current profiles collected from various electric vehicle (EV) driving scenarios and electrochemical states derived from the physics-based model.[15]

The OCV of a battery, in thermodynamic terms, is defined as the difference in electrochemical potential between the two electrodes where no current is flowing.[16] For nickel manganese cobalt (NMC) and nickel cobalt aluminum oxide (NCA) cathodes, the OCV is a monotonic function of SOC. This characteristic is advantageous because it allows for the direct and reliable correlation of the OCV readings with the SOC values. Instead, LFP batteries are characterized by a full cell OCV curve which is flat usually over an SOC range of 30−80%[17] (this can extend up to 20−90% in some cases, see Figure S1). This is the SOC range within which EV batteries commonly operate. This presents a significant challenge for model-based SOC estimation methods, as they rely heavily on the inversion of the OCV−SOC lookup table to infer SOC from voltage measurements. The flatness of the OCV curve in this range reduces the sensitivity of voltage to SOC changes (i.e., $\frac{dOCV}{dSOC} \approx 0$), making it difficult to accurately estimate the SOC based on voltage alone. In model-based methods, a "copy" of the battery dynamics, either in the form of ECMs[18,19] or physics-based electrochemical models,[14,20] is used to design closed loop feedback estimators. Commonly used filters include extended Kalman filter (EKF),[21] unscented Kalman filter (UKF),[22] and adaptive EKF (AEKF).[23,28] However, the flatness of the OCV curve makes traditional OCV-based filtering methods less effective for LFP batteries.

When the battery is at rest or operating at low current levels, the low signal-to-noise ratio of the current measurements further hampers the accurate SOC estimation. Additionally, the path-dependent behavior of LFP batteries causes relaxation voltages for the same SOC to vary depending on previous loading conditions. This makes the OCV−SOC map inversion operation ineffective for accurate SOC estimation, as the voltage response is no longer solely a function of SOC but also influenced by the battery's history.

This study focuses on enhancing the model-free Coulomb counting method. The Coulomb counting method directly calculates battery SOC by integrating the current over time

https://doi.org/10.1021/acsenergylett.4c03223
ACS Energy Lett. 2025, 10, 741−749

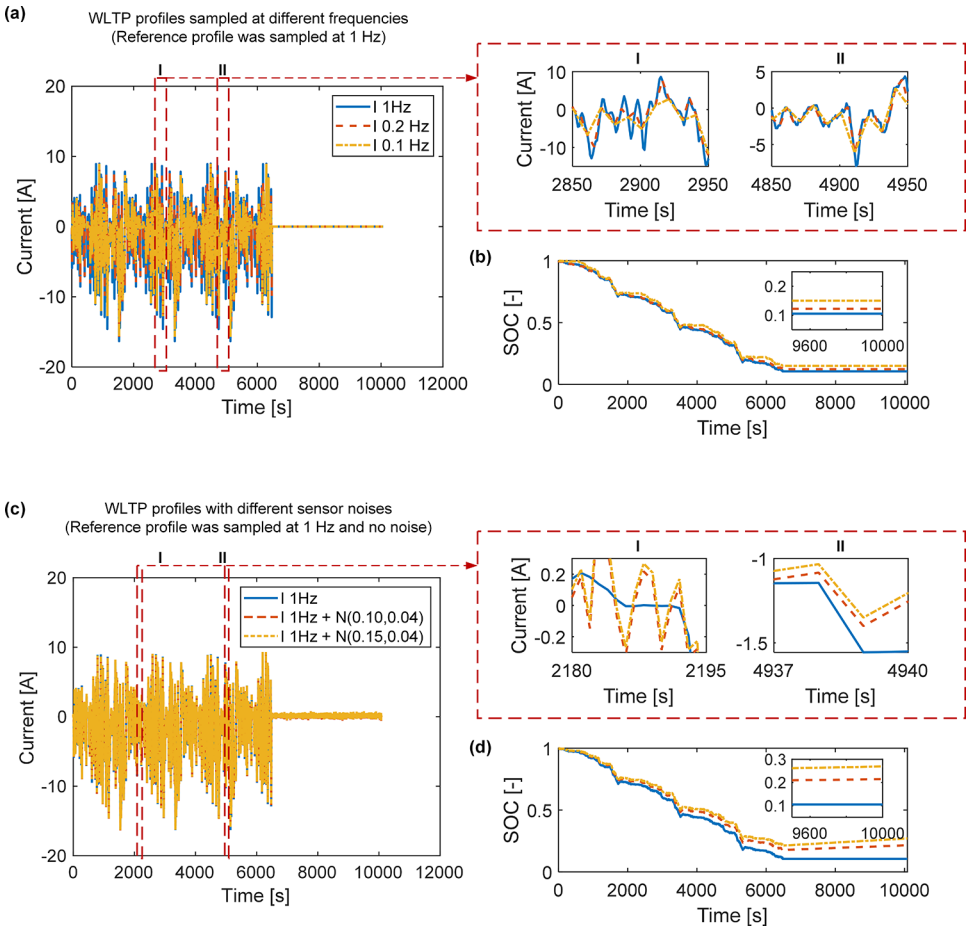

Figure 2. Analysis of error sources due to sampling frequency and sensor noise in the current measurements. (a) Current profiles at different sampling frequencies. The reference profile is the WLTP profile sampled at 1 Hz, then downsampled to 0.2 and 0.1 Hz. The zoomed-in plots illustrate the changes in the current profile as the sampling frequency decreases. (b) SOC calculated by the Coulomb counting method using the downsampled current profiles. SOC error arises when down-sampled profiles are used in the Coulomb counting method. (c) Current profiles with added noise. The reference current profile is the WLTP profile sampled at 1 Hz without noise. Gaussian noise N(0.10,0.04) and N(0.15,0.04) (i.e., variance of 0.04 A and mean of 0.10 A and 0.15 A, respectively) was added to the reference profile. (d) SOC calculated by the Coulomb counting method using current profiles with and without the Gaussian noise.

and is widely used in BMS for onboard SOC estimation due to its low computational requirements.[24] However, despite its simplicity, the accuracy of this method can drift over time due to cumulative integration errors, reliance on precise current measurements, incorrect initialization, and inaccurate capacity estimation, making it less robust in long-term use compared with more sophisticated model-based methods.

The Coulomb counting method is summarized by the following equation:

$$\mathrm{SOC}(t) = \mathrm{SOC}(t_0) - \frac{1}{Q}\int_{t_0}^{t} I(\tau)\mathrm{d}\tau \tag{1}$$

where $\mathrm{SOC}(t_0)$ is the initial SOC calculated by inverting the OCV−SOC map using the measured voltage after the battery has undergone a prolonged rest period, allowing it to reach equilibrium. With this initial condition (i.e., SOC (t_0)), the battery's SOC over time, $\mathrm{SOC}(t)$, is calculated by integrating the current $I(\tau)$. The battery capacity, Q (a function of temperature), serves as a normalization factor in the SOC calculation, ensuring that SOC values accurately represent the available charge as a proportion of the battery's total capacity. In the SOC calculation using the Coulomb counting method, four primary error sources can significantly impact the accuracy of the SOC estimation, as described below.

Wrong Initialization. One common error in the SOC calculation using the Coulomb counting method is incorrect initialization. According to eq 1, the initial SOC, $\mathrm{SOC}(t_0)$, serves as the reference point for subsequent SOC estimation. To determine $\mathrm{SOC}(t_0)$, the measured voltage after a prolonged rest period is typically utilized through the inversion of the OCV−SOC map. Figure 1a shows the voltage and SOC profiles over the Worldwide Harmonized Light Vehicles Test Procedure (WLTP) cycle, followed by a 1 h rest period. The battery starts fully charged at initial SOC of 100% and then is discharged to an SOC of 10% (i.e., solid red line calculated using Coulomb counting). Once the battery reaches 10% SOC, the load is disconnected (zero current) and the voltage relaxes to its equilibrium, OCV. As illustrated in Figure 1a, during the relaxation period, the difference between the voltage and OCV decreases as the rest time increases. However, it is noteworthy that for LFP cells, a discrepancy between the measured voltage and the OCV can still be present even after a 48 h rest period.[9] This persistence of the voltage difference is particularly important because the flatness of the SOC−OCV curve

https://doi.org/10.1021/acsenergylett.4c03223
ACS Energy Lett. 2025, 10, 741−749

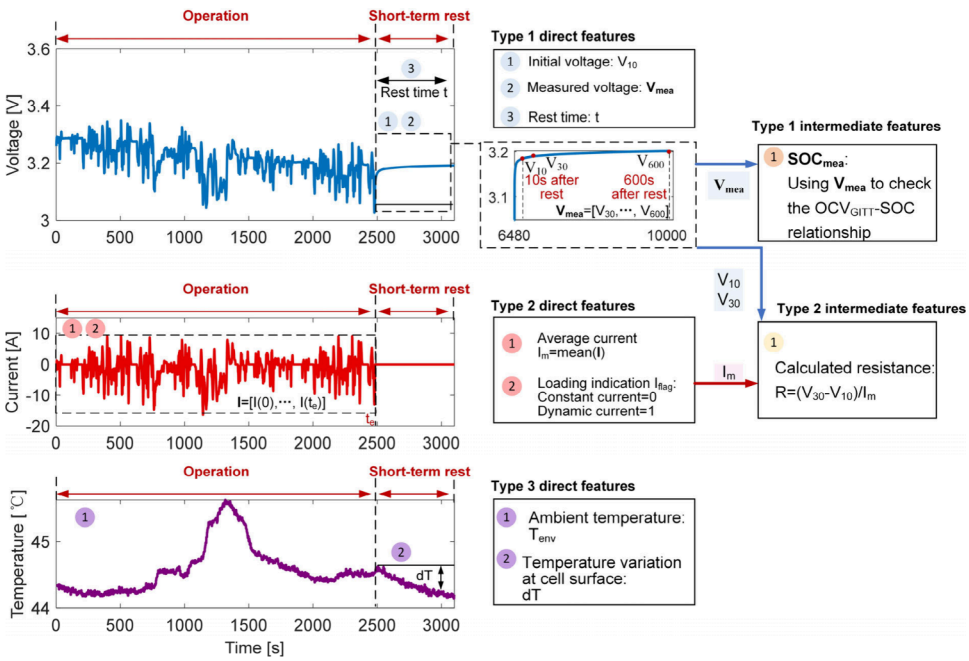

Figure 3. Feature extraction from the voltage, current, and temperature data. The first step in training the machine learning model is feature extraction. In this study, a short-term relaxation period is introduced after charging or discharging the battery. During this rest period, various features are extracted from the measured voltage, current (prior to the rest period), and temperature data. In this study, both direct and intermediate features are extracted. The three types of direct features are type 1 (from voltage measurements), type 2 (from current measurements), and type 3 (from temperature measurements). Intermediate features are then calculated based on these direct features. Specifically, type 1 intermediate features are derived from type 1 direct features, using V_{mea} in the OCV_{GITT}−SOC inversion, while type 2 intermediate features are obtained by combining type 1 and type 2 direct features.

means that even minor variations in voltage readings can lead to significant errors in SOC estimation.

Voltage measurement noise, represented as offsets, can significantly impact the SOC accuracy. In Figure 1b, we analyze how such offset-induced noise on OCV measurements affects SOC estimation derived from OCV_{GITT}−SOC map inversion. Here, OCV_{GITT} refers to the OCV obtained from the Galvanostatic intermittent titration technique (GITT) test (see Figure S1). Effects of offset noise spanning from 5 to 30 mV are analyzed. Figure 1b (inset I) provides a closer look at these errors in the case of an overall offset of 30 mV on the value of the measured voltage of 3.2947 V (corresponding to 40% SOC). An offset of +15 mV added to 3.2947 V induces a voltage reading of 3.3097 V which from the OCV_{GITT}−SOC lookup inversion corresponds to 70.67% SOC (¯(SOC_mea)), whereas an offset of −15 mV leads to a voltage reading of 3.2797 V, hence SOC = 30.81% (¯(SOC_mea)). Even a small 5 mV offset can result in a 20% SOC error. When such errors are used to initialize SOC in the Coulomb counting method, they propagate as SOC offset errors.

Sampling Frequency. Another critical factor affecting SOC estimation accuracy, in both Coulomb counting and model-based methods, is the sampling frequency. To minimize memory usage, the sampling frequency of current and voltage measurements is often reduced in BMS algorithms. For example, according to the Chinese Technical Specifications for the Remote Service and Management System of Electric Vehicles, the data sampling frequency is set at 0.1 Hz.[25] Figure 2a presents the current profile with different sampling frequencies. The reference current profile, shown in blue, is the WLTP profile sampled at 1 Hz. This profile is then downsampled to 0.2 and 0.1 Hz, respectively. As seen in the zoomed-in plot, as the sampling frequency decreases, the shape of the curve profile deviates from the reference current, leading to cumulative errors in current integration, as shown in Figure 2b.

Current Noise. Sensor noise also alters the shape of the current profile. As shown in Figure 2c, two Gaussian noises, each with a variance of 0.04 A and mean values of 0.1 A and 0.15 A were added to the reference WLTP current profile. These current noisy profiles lead to SOC calculation errors when the Coulomb counting method is applied, as illustrated in Figure 2d. Notably, noisy current data leads to more significant SOC errors compared to the downsampled current profile. Further details are provided in Figure S2.

Battery Capacity Degradation. Over long-term operation, battery capacity gradually degrades, which may affect the accuracy of SOC estimation using the Coulomb counting method. However, LFP batteries exhibit a significantly longer cycle life (approximately 4−5 times that of NCA or NMC cathodes[26,27]), resulting in a slower rate of capacity degradation, which can be monitored and calibrated during routine maintenance. Although capacity degradation is not addressed in this study, the framework is designed to incorporate updated capacity values as they become available. In this article, we depart from traditional model-based SOC estimation methods for LFP batteries and propose a novel, model-free machine learning approach. Specifically, we address the main limitation of the Coulomb counting method caused by incorrect initialization. To overcome this, we employ a machine-learning-based approach that refines the initial SOC guess using voltage and temperature time series during relaxation periods (when the current is zero) and leverages

https://doi.org/10.1021/acsenergylett.4c03223
ACS Energy Lett. 2025, 10, 741−749

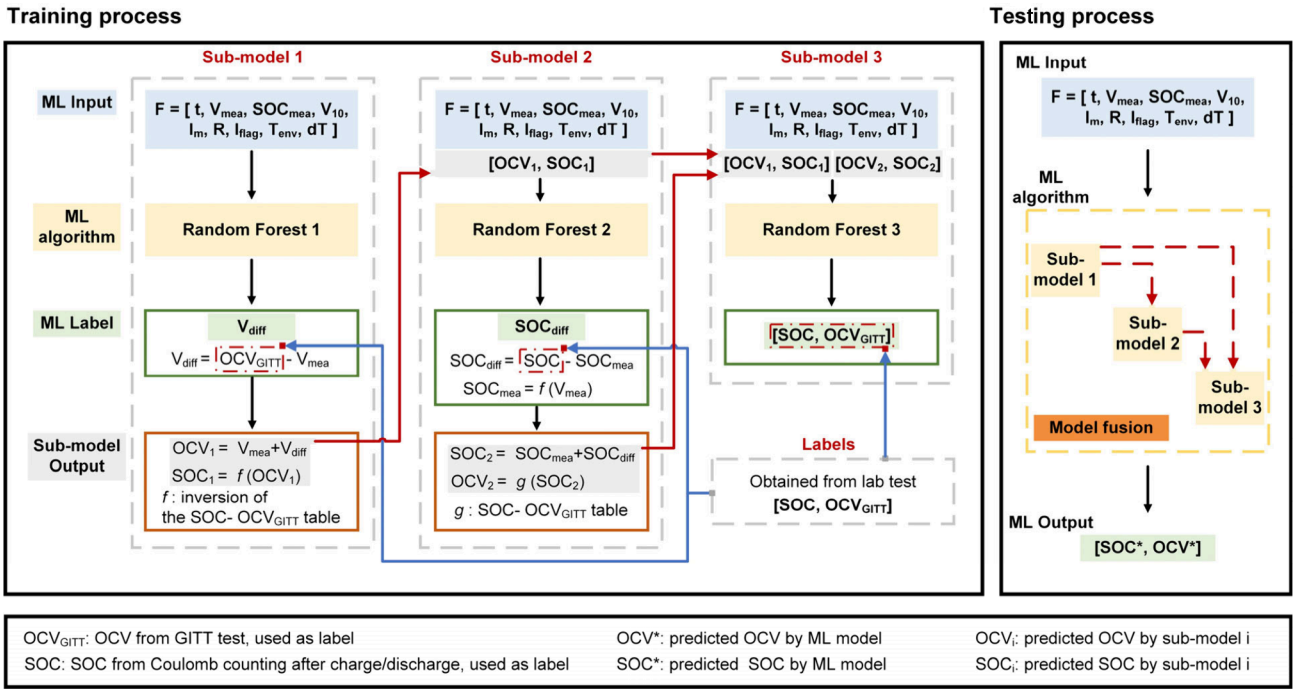

Figure 4. Flowchart of the proposed machine learning pipeline for onboard battery SOC resetting. Based on the extracted features, a machine-learning pipeline consisting of three submodels is built to correct battery initial SOC. In submodel 1, using extracted feature vector F as the input, the label for random forest 1 is the voltage difference V_{diff}. Then, submodel 1 generates OCV_1 and SOC_1. In submodel 2, both the feature vector F, OCV_1, and SOC_1 are taken as inputs, and the label for random forest 2 is the SOC difference SOC_{diff}. After that, submodel 2 outputs SOC_2 and OCV_2. Finally, in submodel 3, the feature vectors F, SOC_1, OCV_1, SOC_2, and OCV_2 are used as inputs and OCV_{GITT} and SOC (calculated from Coulomb counting after discharge/charge) are used as the training labels. During the testing process, the feature vector F extracted from both the short-term relaxation period and historical current data is used as input for the trained machine learning model, which gives the estimated SOC, SOC*, and estimated OCV, OCV*, of the cell.

historical current data (see Supplementary Note 1 for more details).

The feature vector ($\mathbf{F} = [t, V_{mea}, SOC_{mea}, V_{10}, I_m, R, I_{flag}, T_{env}, dT]$, see Table S1 for detailed descriptions) is extracted from current historical data (collected before the battery goes to rest) as well as the voltage and temperature measurements time series at a low sampling frequency during rest, as shown in Figure 3. These extracted features are then used to train the machine learning model according to the pipeline shown in Figure 4, which includes the creation of three submodels. Taking the feature vector **F** as input, the label for submodel 1 is V_{diff}, defined as the difference between measured voltage, V_{mea} (taken at 30 s intervals from 30 to 600 s), and OCV_{GITT}. Submodel 1 then generates OCV_1 (calculated as $V_{diff} + V_{mea}$) and SOC_1 (obtained from OCV_{GITT}−SOC map inversion using OCV_1). Next, submodel 2 takes the feature vector **F**, OCV_1, and SOC_1 (from submodel 1) as inputs and uses SOC_{diff}, defined as the difference between real SOC (calculated from Coulomb counting after charge/discharge the cell) and SOC_{mea}, as the label. Here, SOC_{mea} is obtained from the OCV_{GITT}−SOC map inversion using V_{mea}. Submodel 2 generates SOC_2 (defined as $SOC_{mea} + SOC_{diff}$) and OCV_2 (from OCV_{GITT}−SOC map interrogation using SOC_2). Finally, submodel 3 uses the feature vector **F**, SOC_1 and OCV_1 from submodel 1, and SOC_2 and OCV_2 from submodel 2 as inputs to estimate battery SOC (SOC*) and OCV (OCV*).

For real time applications, the trained model takes the extracted features from a short-term relaxation (i.e., voltage and temperature data) and historical current data and outputs both the estimated OCV, OCV*, and estimated SOC, SOC*. In the proposed method, voltage and temperature features are extracted during rest periods ranging from 30 to 600 s (at 30 s intervals, with an additional voltage point V_{10} measured at 10 s after the load is disconnected). These periods are termed short-term rest in this study. Additionally, the current features are calculated from historical data.

The machine learning pipeline proposed in this study enables accurate and rapid SOC resetting during short-term voltage relaxation, making it a promising and easy to implement solution for BMS applications. The proposed pipeline performs effectively with low sampling frequency voltage and temperature data (1/30 Hz) and historical current data (the sampling frequency has minimal impact provided the mean current value is utilized) and has been experimentally validated across 434 different working conditions (see Figure S3, Figure S4, and Supplementary Note 2).

Battery experimental data sets are essential for developing battery models and state estimation algorithms. In this study, we developed a comprehensive design of experiments (DOE) and conducted testing at the Stanford Energy Control Laboratory (Figure S5) on cylindrical 26650 LFP/graphite cells (Table S2). The data set includes 434 testing conditions (Supplementary Note 2) across eight battery cells (Figure S3). The experiments were specifically designed to capture resting voltage segments under a wide range of loading (constant and dynamics) and temperature conditions, in both charge and discharge. Tests included capacity tests (Supplementary Note 3), OCV tests (Figure S1), and training/validation tests (Figure S3). Tests for cells 1 to 6 were conducted at 10, 25,

https://doi.org/10.1021/acsenergylett.4c03223
ACS Energy Lett. 2025, 10, 741−749

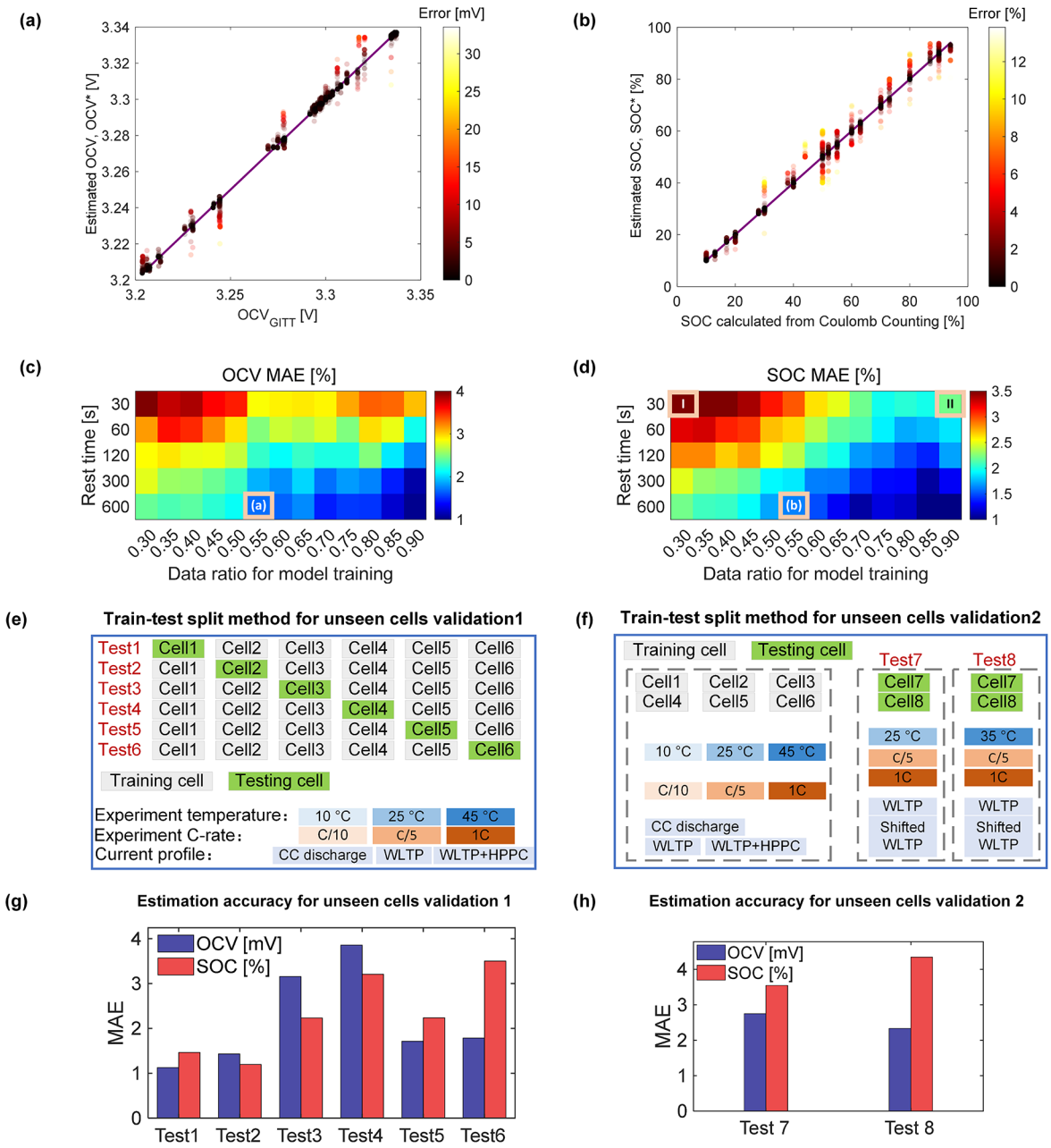

Figure 5. Validation of the proposed machine learning pipeline. Estimation accuracy using data obtained after 10 min rest. The case split strategy was employed to generate the train−test split. The data ratio for training is 0.55, and the data ratio for testing is 0.45. (a) Parity plots for estimated OCV* and OCV_{GITT}. (b) Parity plot for estimated SOC* and SOC calculated from Coulomb counting. Estimation accuracy using data from rest periods ranging from 30 to 600 s. Case split was applied to create training−test splits, with training data ratios varying from 0.3 to 0.9 (corresponding testing data ratios ranging from 0.7 to 0.1). (c) MAE of the estimated OCV*. (d) MAE of the estimated SOC*. (e) Testing design for the first type of unseen cell validation including cells 1 to 6. (f) Testing design for the second type of unseen cell validation including cells 7 and 8. (g) Estimation accuracy for OCV* and SOC* under unseen cells validation 1. (h) Estimation accuracy for OCV* and SOC* under unseen cells validation 2.

and 45 °C, while tests for cells 7 and 8 were performed at 25 and 35 °C. During testing, cells were subjected to different current profiles across the full SOC range (i.e., from 0% to 100% SOC) with a 1 h rest period after each charge or discharge to a designated SOC.

In the capacity tests, the batteries are fully charged and discharged using constant current (CC) profiles at C/5. The C/5 test data is then used to calculate the battery's nominal capacity (Supplementary Note 3). In this work, the reference OCV (i.e., OCV_{GITT}) is derived from GITT tests. During the GITT test, the battery is discharged from 100% SOC (corresponding to 3.6 V) to 0% SOC (corresponding to 2 V) or charged from 0% SOC (2.8 V) to 100% SOC (3.6 V) at a C/5 rate, in 2.5% SOC increments, followed by a 2 h rest period after each step. In this work, the GITT−OCV curves are compared with the pseudo-OCV curves obtained at C/30 (see Figure S1). Given the differences observed between those two curves, using pseudo-OCV as the benchmark for the inversion of the OCV−SOC leads to errors in the SOC calculation. In the training/validation tests for cells 1 to 6, the

https://doi.org/10.1021/acsenergylett.4c03223
ACS Energy Lett. 2025, 10, 741−749

Table 1. Comparison of OCV and SOC Obtained after a 10 min Rest, Directly Using Measured Data and Estimated by the Proposed Machine Learning Method

	OCV			SOC		
data set generation	method	MAE (mV)	RMSE (mV)	method	MAE (%)	RMSE (%)
case spilt	directly using V_{mea}	16.566	19.972	using V_{mea} for OCV_{GITT}−OCV inversion for SOC_{mea}	12.665	15.480
	using proposed method to estimate OCV*	1.701	3.502	using proposed method to estimate SOC*	1.629	2.942
data spilt	directly using V_{mea}	15.983	19.393	using V_{mea} for OCV_{GITT}−OCV inversion SOC_{mea}	13.228	16.004
	using proposed method to estimate OCV*	0.462	1.981	using proposed method to estimate SOC*	0.588	1.785

batteries are discharged using CC, WLTP, and hybrid pulse power characterization (HPPC) + WLTP profiles to different SOC levels, followed by a 1 h rest period (see Supplementary Note 3) and charged using CC at different C-rate. Data collected from cells 7 and 8 are used to validate the SOC resetting algorithm under "unseen cell scenarios".

We used two split strategies, case split and data split, to create the training and testing data sets for the machine learning model (see Figure S3b). Each case is defined by combining data from a specific temperature, C-rate, current profile, and rest SOC point, as shown in the first column of Figure S3b. For each case, the feature vector **F** was extracted from voltage and temperature measurements every 30 s during the rest period (from 30 to 600 s) and from historical current data before resting. In the case split scenario, the feature vector **F** extracted from the same case is assigned exclusively to either the training or testing data set. In contrast, the data split strategy randomly assigns feature vector **F** from all cases between the training and testing data sets. For example, in the case split scenario, data collected at intervals from 30 to 600 s (every 30 s) from the cell discharged to 30% SOC at 25 °C using an average 1C WLTP profile is assigned to the training data set. In contrast, data (at 30 s intervals from 30 to 600 s) from the cell discharged to 30% SOC at 25 °C using an average 0.5C WLTP profile is assigned to the testing data set. In the data split scenario, data extracted at 30 s from the cell discharged to 30% SOC at 25 °C using an average 1C WLTP profile is used as the training data set, while data extracted at 60 s from the cell tested under the same condition is used as the testing data set.

The data generated in this study can be accessed through the following link: https://github.com/LeXuSECL/ML_SOC_Estimation_ACS_Energy_Letters.

The voltage difference between the OCV_{GITT} and the measured voltage V_{mea}, caused by polarization, can be significant during the first 10 min of rest after the operational current is removed. Figure S6a shows the difference between V_{mea} and OCV_{GITT} during a 10 min relaxation period with a 30 s sampling interval (i.e., 20 entry vector). Significant SOC estimation errors are observed when using the OCV_{GITT}−SOC inversion based on V_{mea}. This challenge is escalated when the battery is traveling over SOC ranges within the flat region of the OCV−SOC curve, as shown in Figure S6b. For example, within the SOC range of 40% to 70%, 58.3% of all cases exhibit SOC estimation errors exceeding 20% when using V_{mea} obtained from a 10 min rest in the OCV_{GITT}−SOC look-up table inversion.

The validation results of the proposed SOC resetting method are shown in Figure 5. Figures 5a and 5b present the errors of estimated OCV, OCV*, and estimated SOC, SOC*, using features extracted after a 10 min rest. Using the case split strategy for train−test data set split (data from cells 1 to 6), the data ratio for training is 0.55 and the data ratio for testing is 0.45. It can be seen from Figures 5a and 5b that most estimatedOCV* errors are below 5 mV (91.7% of the points) and most estimated SOC* errors are below 5% (89.0% of the points). The cumulative density for SOC* and OCV* estimation errors is given in Figure S7. Besides, a few high-error estimation points exist (e.g., 0.14% of the SOC estimation points exceed 12% error) in Figures 5a and 5b. One approach to further reduce these high-error points is to fix the rest time for feature extraction (e.g., only use data after 10 min rest), as detailed in Supplementary Note 4. The mean absolute error (MAE) and root-mean-square error (RMSE) (Supplementary Note 5) for all of the estimation points in Figures 5a and 5b are listed in Table 1. Also, these values are compared with results without using the proposed machine learning method (i.e., V_{mea} after 10 min rest is used to obtain SOC_{mea} from OCV_{GITT}−SOC inversion). It can be seen that the MAE for SOC exceeds 12% before using machine learning and is reduced to less than 2.0% after machine learning correction.

Besides, we ran the above validation 10 times, and the results for the best and worst estimation are shown in Figure S8. The results indicate that there are no significant differences between the best and worst conditions, demonstrating the reliability of the proposed method. More importantly, the proposed method is generally applicable with various machine learning models (details are provided in Supplementary Note 6). The above results were obtained using the case split strategy to generate the training and testing data sets. Additionally, the validation of the proposed machine learning method using data sets from the data split strategy is shown in Table 1 and Figure S9. It can be seen that the MAE of predicted SOC* is less than 0.6%.

To evaluate the performance of the proposed machine learning pipeline more comprehensively, we investigated its accuracy across three different use cases.

Voltage Obtained from Different Relaxation Times. Figures 5a and 5b present the estimation accuracy using features extracted after a 10 min rest. However, features from shorter rest times can also be used in the proposed machine learning pipeline when such long rest time data is unavailable in real-world applications (i.e., waiting for the red light). Using data from cells 1 to 6, and using case split to generate the testing and validation data sets, the proposed machine learning method is validated using features from rest periods ranging from 30 to 600 s. Figures 5c and 5d show the MAE of the estimated OCV and SOC. Each block in Figures 5c and 5d represents the estimation for a specific combination of split

https://doi.org/10.1021/acsenergylett.4c03223
ACS Energy Lett. 2025, 10, 741−749

ratio and rest time (i.e., blocks a and b correspond to the MAE for Figure 5a and Figure 5b, respectively). The results indicate that even with a rest period of just 30 s and using only 30% of the training data set, the estimation error for battery SOC is less than 3.5% (block I). When more training data is available, the SOC estimation error reduces to 2% (block II). Besides, if longer rest voltage data are available, the estimation error for both the OCV and SOC can be below 1%, even with only 30% of the training data (see Figure S10). Moreover, as shown in Figures 5c and 5d, the estimation accuracy of the proposed method improves with increased training data and the use of features extracted from longer rest periods. For instance, when the SOC resetting algorithm is first deployed in a BMS, features should be extracted from long rest periods (e.g., at least 10 min) to ensure high accuracy. As the BMS continues to operate and more data are collected to train the algorithm, the required rest time for feature extraction can be gradually reduced.

Prediction Accuracy over Unseen Cells. To further validate the accuracy of the proposed machine-learning-based SOC estimation method, we tested its performance on data from unseen cells. We conducted two types of unseen cell validations.

In the first validation, data from cells 1 to 6 are used. As shown in Figure 5e, six different unseen cell tests were designed. In each test, data from five cells (shown in gray) were all used in training, and data from the remaining cell (shown in green) was used for testing. Figure 5g illustrates the accuracy of estimated OCV, OCV*, and estimated SOC, SOC*, after the proposed method. In Figure 5g, features were extracted using 10 min relaxation data, and each column in the figure represents one test in Figure 5e. For instance, the first column in Figure 5g indicates that cells 2−6 were used as training cells, while cell 1 was used as the testing cell. The MAE for the OCV and SOC are consistently below 4 mV and 4%, respectively.

In the second validation scenario, additional experiments were conducted using two new cells, 7 and 8 (Figure S3). The machine learning model was first trained on the entire data set from cells 1 to 6 and then tested on the data sets from cells 7 and 8 (referred to as test 7 and test 8 in Figure 5f). In test 7, the experiment's C-rates and temperature were included in the training data set, but unseen current profiles (i.e., the shifted WLTP profile described in Figure S4's caption) were used for data generation. Therefore, test 7 represents a validation with both unseen cells and unseen profiles. Moreover, test 8 contains both one unseen temperature (i.e., 35 °C) and one unseen profile (shifted WLTP). Estimation accuracy for tests 7 and 8 is shown in Figure 5h and Figure S11. It can be seen that the estimated OCV, OCV*, and estimated SOC, SOC*, have high accuracy, with errors below 3 mV and 4.3%, respectively.

Effects of Noise. Finally, the influence of noise on the model accuracy is considered. In real applications, the quality of measured voltage data is generally lower than that obtained under laboratory test conditions due to sensor noise. To evaluate the robustness of the proposed machine learning pipeline, we introduced Gaussian noise with different standard deviations into the experimental data.

$$V_{\text{use}} = V_{\text{mea}} + V_{\text{Gaussian}} \tag{2}$$

where $v_{\text{Gaussian}} \approx \text{N}(\mu, \sigma^2)$ is the Gaussian noise with mean μ and variance σ^2, where μ varies from −2.5 to 2.5 mV and σ from 0 to 2.5 mV. Across all noise conditions, the prediction MAEs for voltage remained below 2 mV, and the MAEs for SOC estimation stayed below 3.5% (see Figure S12 for more details). These results indicate that the proposed method exhibits strong resilience to noise, highlighting its potential for practical applications.

Accurate SOC estimation for LFP batteries is critical for the safe and reliable operation of the battery systems. Traditional model-based SOC estimation methods often face challenges, such as hysteresis, path dependence, and flat OCV issues. This paper proposes a machine-learning-based solution to address the above challenges by accurately resetting the SOC in Coulomb counting by utilizing relaxation data during a short resting time using a low sampling frequency. This approach ensures rapid and efficient SOC resetting for onboard BMS estimation.

Experiments were designed and conducted for training, validation and test under various scenarios. For the first time, SOC error sources are quantitatively analyzed, providing valuable insights for the development of SOC estimation methods for real-world applications. Data show that SOC errors caused by inaccurate voltage measurements are significant for LFP batteries due to the flat OCV−SOC curve. For instance, a 5 mV offset voltage error can result in SOC estimation errors exceeding 20%. Validation results demonstrate that using data obtained from a 1 min voltage relaxation period, the MAE of the predicted OCV and SOC by the proposed pipeline are less than 3 mV and 2.5%, respectively. The generalizability of the pipeline was proven by various machine learning algorithms. The robustness of the pipeline was further validated using training data from different time scales, unseen conditions, and with added noise. These results indicate the potential of this method for adoption in onboard applications. In addition to SOC estimation, the proposed machine learning framework can also be extended to estimate battery state-of-health. For instance, in addition to features from the relaxation period, peak shifting values derived from incremental capacity analysis or differential voltage analysis conducted at different aging stages can be incorporated as input features. The machine learning algorithm can then output both the battery's SOC and capacity.

■ ASSOCIATED CONTENT

Data Availability Statement

The raw data generated in this study can be accessed at:https://github.com/LeXuSECL/ML_SOC_Estimation_ACS_Energy_Letters

Supporting Information

The Supporting Information is available free of charge at https://pubs.acs.org/doi/10.1021/acsenergylett.4c03223.

Loading (current), voltage and temperature profiles for GITT and pseudo-OCV tests, additional results on sampling frequency effects on SOC estimation accuracy, experiment design and platform details, cumulative error distributions, results with split data sets, varying rest times and training data ratios, unseen test results, validations with voltage noise, detailed machine learning descriptions, experimental procedures, and error reduction strategies (PDF)

https://doi.org/10.1021/acsenergylett.4c03223
ACS Energy Lett. 2025, 10, 741−749

AUTHOR INFORMATION

Corresponding Authors

Xiaosong Hu − *College of Mechanical and Vehicle Engineering, Chongqing University, Chongqing 40044, China*; Email: xiaosonghu@ieee.org

Simona Onori − *Department of Energy Science and Engineering, Stanford University, Stanford, California 94305, United States*; Email: sonori@stanford.edu

Authors

Yunhong Che − *Department of Energy Science and Engineering, Stanford University, Stanford, California 94305, United States; Department of Energy, Aalborg University, Aalborg 9220, Denmark*

Le Xu − *Department of Energy Science and Engineering, Stanford University, Stanford, California 94305, United States*; orcid.org/0000-0001-5114-1119

Remus Teodorescu − *Department of Energy, Aalborg University, Aalborg 9220, Denmark*

Complete contact information is available at: https://pubs.acs.org/10.1021/acsenergylett.4c03223

Author Contributions

[§]Y.C. and L.X. contributed equally.

Notes

[○]Y.C. was a visiting scholar at the Department of Energy Science and Engineering, Stanford University, 367 Panama Street, Stanford, CA 94305, USA at the time of this research was conducted.

The authors declare no competing financial interest.

REFERENCES

(1) Pozzato, G.; et al. Analysis and key findings from real-world electric vehicle field data. *Joule* **2023**, *7*, 2035−2053.

(2) Albertus, P.; Manser, J. S.; Litzelman, S. Long-Duration Electricity Storage Applications, Economics, and Technologies. *Joule* **2020**, *4*, 21−32.

(3) Longchamps, R. S.; Yang, X.-G.; Wang, C.-Y. Fundamental Insights into Battery Thermal Management and Safety. *ACS Energy Lett.* **2022**, *7*, 1103−1111.

(4) Schöberl, J.; Ank, M.; Schreiber, M.; Wassiliadis, N.; Lienkamp, M. Thermal runaway propagation in automotive lithium-ion batteries with NMC-811 and LFP cathodes: Safety requirements and impact on system integration. *eTransportation* **2024**, *19*, 100305.

(5) Zhang, Z.; et al. A comparative study of the LiFePO4 battery voltage models under grid energy storage operation. *J. Energy Storage* **2024**, *75*, 109696.

(6) Degen, F.; Winter, M.; Bendig, D.; Tübke, J. Energy consumption of current and future production of lithium-ion and post lithium-ion battery cells. *Nat. Energy* **2023**, *8*, 1284−1295.

(7) Rahimi-Eichi, H.; Ojha, U.; Baronti, F.; Chow, M.-Y. Battery Management System: An Overview of Its Application in the Smart Grid and Electric Vehicles. *IEEE Ind. Electron. Mag.* **2013**, *7*, 4−16.

(8) Hannan, M. A.; Lipu, M. S. H.; Hussain, A.; Mohamed, A. A review of lithium-ion battery state of charge estimation and management system in electric vehicle applications: Challenges and recommendations. *Renew. Sustain. Energy Rev.* **2017**, *78*, 834−854.

(9) Dreyer, W.; et al. The thermodynamic origin of hysteresis in insertion batteries. *Nat. Mater.* **2010**, *9*, 448−453.

(10) Ovejas, V. J.; Cuadras, A. Effects of cycling on lithium-ion battery hysteresis and overvoltage. *Sci. Rep.* **2019**, *9*, 14875.

(11) Plett, G. L. *Battery Management Systems, Vol. II: Equivalent-Circuit Methods*; Artech House, 2015.

(12) Plett, G. L. Extended Kalman filtering for battery management systems of LiPB-based HEV battery packs: Part 2. Modeling and identification. *J. Power Sources* **2004**, *134*, 262−276.

(13) Gao, Y.; Plett, G. L.; Fan, G.; Zhang, X. Enhanced state-of-charge estimation of LiFePO4 batteries using an augmented physics-based model. *J. Power Sources* **2022**, *544*, 231889.

(14) Pozzato, G.; et al. Core-Shell Enhanced Single Particle Model for lithium iron phosphate Batteries: Model Formulation and Analysis of Numerical Solutions. *J. Electrochem. Soc.* **2022**, *169*, 063510.

(15) Pozzato, G.; Li, X.; Lee, D.; Ko, J.; Onori, S. Accelerating the transition to cobalt-free batteries: a hybrid model for LiFePO4/graphite chemistry. *Npj Comput. Mater.* **2024**, *10*, 14.

(16) Newman, J.; Balsara, N. P. *Electrochemical Systems*; John Wiley & Sons, 2021.

(17) Zhang, X.; Peng, H.; Wang, H.; Ouyang, M. Hybrid Lithium Iron Phosphate Battery and Lithium Titanate Battery Systems for Electric Buses. *IEEE Trans. Veh. Technol.* **2018**, *67*, 956−965.

(18) Lai, X.; Wang, S.; Ma, S.; Xie, J.; Zheng, Y. Parameter sensitivity analysis and simplification of equivalent circuit model for the state of charge of lithium-ion batteries. *Electrochim. Acta* **2020**, *330*, 135239.

(19) Naseri, F.; Schaltz, E.; Stroe, D.-I.; Gismero, A.; Farjah, E. An Enhanced Equivalent Circuit Model With Real-Time Parameter Identification for Battery State-of-Charge Estimation. *IEEE Trans. Ind. Electron.* **2022**, *69*, 3743−3751.

(20) Xu, L.; Lin, X.; Xie, Y.; Hu, X. Enabling high-fidelity electrochemical P2D modeling of lithium-ion batteries via fast and non-destructive parameter identification. *Energy Storage Mater.* **2022**, *45*, 952−968.

(21) Li, J.; Klee Barillas, J.; Guenther, C.; Danzer, M. A. A comparative study of state of charge estimation algorithms for LiFePO4 batteries used in electric vehicles. *J. Power Sources* **2013**, *230*, 244−250.

(22) He, H.; Qin, H.; Sun, X.; Shui, Y. Comparison Study on the Battery SoC Estimation with EKF and UKF Algorithms. *Energies* **2013**, *6*, 5088−5100.

(23) Taborelli, C.; Onori, S.. State of charge estimation using extended Kalman filters for battery management system. In *2014 IEEE International Electric Vehicle Conference (IEVC)* ; IEEE, 2014; pp 1−8. DOI: 10.1109/IEVC.2014.7056126.

(24) Adaikkappan, M.; Sathiyamoorthy, N. Modeling, state of charge estimation, and charging of lithium-ion battery in electric vehicle: A review. *Int. J. Energy Res.* **2022**, *46*, 2141−2165.

(25) Hao, X.; Wang, H.; Lin, Z.; Ouyang, M. Seasonal effects on electric vehicle energy consumption and driving range: A case study on personal, taxi, and ridesharing vehicles. *J. Clean. Prod.* **2020**, *249*, 119403.

(26) Zhao, T.; et al. An overview on the life cycle of lithium iron phosphate: synthesis, modification, application, and recycling. *Chem. Eng. J.* **2024**, *485*, 149923.

(27) Dechent, P.; et al. ENPOLITE: Comparing Lithium-Ion Cells across Energy, Power, Lifetime, and Temperature. *ACS Energy Lett.* **2021**, *6*, 2351−2355.

(28) Gao, Y.; Nguyen, T.; Onori, S. Model-Based State-of-Charge Estimation of 28 V LiFePO4 Aircraft Battery. *SAE Int. J. Elec. Veh.* **2025**, *14* (1), n/a.